ELSEVIER

Journal of Quantitative Spectroscopy & Radiative Transfer 92 (2005) 189–200

Journal of Quantitative Spectroscopy & Radiative Transfer

www.elsevier.com/locate/jqsrt

An efficient diffusion approximation for 3D radiative transfer parameterization: application to cloudy atmospheres

Y. Chen, K.N. Liou*, Y. Gu

Department of Atmospheric Sciences, University of California, Los Angeles, CA 90095, USA

Received 8 March 2004; accepted 30 July 2004

Abstract

The three-dimensional (3D) diffusion radiative transfer equation, which utilizes a four-term spherical harmonics expansion for the scattering phase function and intensity, has been efficiently solved by using the full multigrid numerical method. This approach can simulate the transfer of solar and thermal infrared radiation in inhomogeneous cloudy conditions with different boundary conditions and sharp boundary discontinuity. The correlated *k*-distribution method is used in this model for incorporation of the gaseous absorption in multiple-scattering atmospheres for the calculation of broadband fluxes and heating rates in the solar and infrared spectra. Comparison of the results computed from this approach with those computed from plane-parallel and 3D Monte Carlo models shows excellent agreement. This 3D radiative transfer approach is well suited for radiation parameterization involving 3D and inhomogeneous clouds in climate models.

Keywords: 3D radiative transfer; Diffusion approximation; Multigrid method; Clouds

1. Introduction

Clouds, which occupy more than 50% of the sky, are generally finite and inhomogeneous. They are the most important element in modulating the energy budget of the earth–atmosphere system

*Corresponding author. Tel.: +1-310-825-5039; fax: +1-310-267-2252.
E-mail address: knliou@atmos.ucla.edu (K.N. Liou).

0022-4073/$ - see front matter © 2004 Elsevier Ltd. All rights reserved.
doi:10.1016/j.jqsrt.2004.07.029

and hence climate. The potential effects of cloud geometry and inhomogeneity on the transfer of radiation must be carefully studied to understand their impact on the radiative properties of the atmosphere as well as to perform proper interpretations of radiometric measurements from the ground, the air, and space. Moreover, incorporation of these effects on radiative transfer in climate and general circulation models (GCMs) remains one of the most difficult problems due to the complexity of cloud formation treatment in the model and the associated radiative transfer calculations. All GCMs at present consider clouds to be plane-parallel and homogeneous with respect to radiation calculations. However, several studies have shown that the inhomogeneity effects are significant in overcast clouds [1] and potentially large in broken cloud fields [2–5].

Several methods have been developed for the calculation of the transfer of radiation in three-dimensional (3D) domain based on a spherical-harmonics method in multiple dimensions for thermal infrared and solar radiative transfer [6,7]. Radiative transfer in 2D inhomogeneous cloud fields was studied by using a spherical-harmonics method [8] and a Fourier-Riccati approach [9]. Liou and Rao [10] presented a successive-orders-of-scattering approach, which can be directly applied to specific geometry and inhomogeneous structure of a medium, for application to cirrus clouds. Evans [11] utilized a spherical harmonics discrete-ordinates method to model radiative transfer in inhomogeneous 3D media. More recently, Gu and Liou [5] developed a 3D inhomogeneous radiative transfer model based on a modified diffusion approximation employing the Cartesian coordinates, specifically for application to climate models.

In Gu and Liou's model, the diffusion approximation for the basic radiative transfer equation was solved by the successive over-relaxation method. While this numerical approach is generally adequate in terms of accuracy, we encounter difficulty at the sharp internal interface. For this reason, we have further developed a more efficient method based on the full multigrid numerical approach to obtain a numerical solution for the inhomogeneous partial differential diffusion equation in which different boundary conditions can be imposed. This paper is organized as follows. Section 2 presents the 3D inhomogeneous radiative transfer model, including basic equations and different boundary conditions for solar and thermal infrared radiation. In Section 3, we discuss the full multigrid method that numerically solves the 3D inhomogeneous diffusion equation. In Section 4, we provide a general check of the accuracy of the present multigrid method by comparison with the results computed from the plane-parallel and Monte Carlo methods. Finally, conclusions are given in Section 5.

2. Diffusion approximation for radiative transfer

2.1. Diffusion approximation equation

The general steady-state radiative transfer equation for diffuse intensity I in 3D space can be expressed in the form [12]

$$-\frac{1}{\beta_e(\mathbf{s})}(\mathbf{\Omega}\cdot\nabla)I(\mathbf{s},\mathbf{\Omega}) = I(\mathbf{s},\mathbf{\Omega}) - J(\mathbf{s},\mathbf{\Omega}), \tag{1}$$

where $\mathbf{s}$ is the position vector; $\mathbf{\Omega}$ is the scattering angular direction vector at $\mathbf{s}$; and β_e, the extinction coefficient, is also a function of the position vector. The source function term J includes single scattering of the direct solar irradiance, multiple scattering of the diffuse intensity, and thermal emission. Expanding the phase function P and the intensity I in terms of the spherical harmonic functions [7,8] in the Cartesian coordinates and taking first four terms, the so-called *diffusion approximation*, the 3D inhomogeneous diffusion equation for radiative transfer can be derived as follows [5,12]:

$$\nabla \cdot (\nabla I_0^0/\beta_t) - 3\alpha_t I_0^0 = -F_t + \mathbf{\Omega}_0 \cdot \nabla(F_t g/\beta_t), \tag{2}$$

where

$$\beta_t = \beta_e(1 - \varpi g),$$
$$\alpha_t = \beta_e(1 - \varpi),$$
$$F_t = \begin{cases} 3\beta_e \varpi F_0 e^{-\tau_s}/4\pi & \text{solar,} \\ 3\beta_e(1-\varpi)B(T) & \text{IR.} \end{cases}$$

In these equations, all the variables are functions of the coordinate (x, y, z); $\varpi = \beta_s/\beta_e$ is the single-scattering albedo; $\mathbf{\Omega}_0$ is the incident solar angular direction vector; F_0 is the incident solar irradiance; τ_s is the optical depth in the direction of the incident solar beam; $B(T)$ is the Planck function of temperature T; I_0^0 is the first component of the intensity expansion; g is the asymmetry factor; and F_t is associated with the direct solar radiation and thermal emission depending on the wavelength. For thermal infrared radiation transfer, the last term in Eq. (2) vanishes.

Once we obtain I_0^0 from Eq. (2), which can be solved numerically, the diffuse intensity and fluxes can be expressed as follows:

$$I(x, y, z; \mathbf{\Omega}) = I_0^0(x, y, z) - \frac{3}{2h\beta_e} \sum_{j=1}^{3} \frac{\partial I_0^0}{\partial x_j} \Omega_{x_j} + \frac{9q}{2h} (\mathbf{\Omega} \cdot \mathbf{\Omega}_0) e^{-\tau_s}, \tag{3}$$

$$F_{\pm x_i}(x, y, z) = \int_{2\pi} I(x, y, z; \mathbf{\Omega}) \Omega_{x_i} \, d\Omega, \tag{4}$$

where $x_1 = x$, $x_2 = y$, $x_3 = z$; $h = 3(1 - \varpi g)/2, q = \varpi g F_0/12\pi$; $\Omega_x = (1 - \mu^2)^{1/2} \cos\phi$, $\Omega_y = (1 - \mu^2)^{1/2} \sin\phi$ and $\Omega_z = \mu$. For thermal infrared radiation, the last term in Eq. (3) can be removed.

2.2. Boundary conditions

2.2.1. Solar radiation boundary conditions

The upward/downward fluxes $F_z^{\uparrow\downarrow}$ can be obtained from Eq. (4) through the angular integration over upward and downward hemispheres, i.e., $(0, 2\pi)$ for ϕ and $(0, \pm 1)$ for μ in the form

$$F_z^{\uparrow\downarrow} = \pi I_0^0 \pm \frac{\pi}{h\beta_e} \frac{\partial I_0^0}{\partial z} \mp \frac{3q}{h} \pi \mu_0 e^{-\tau_s}. \tag{5}$$

The vertical boundary conditions can be expressed in the form

$$\left[\frac{\partial I_0^0}{\partial z} + e_z I_0^0\right]_{z=\binom{0}{z^*}} = f_{z=\binom{0}{z^*}}, \tag{6}$$

where $z = 0$ represents the top of the domain, $z = z^*$ denotes the lower boundary. If a constant incident downward diffuse flux $F_{\text{top}}^{\downarrow}$ is allowed and the lower surface albedo is denoted as $\sigma(x, y)$, the coefficients e_z and f_z in Eq. (6) can be derived as follows:

$$e_{z=0} = -h\beta_e, \quad f_{z=0} = 3q\beta_e\mu_0 e^{-(\tau_{z=0})} + \frac{h\beta_e F_{\text{top}}^{\downarrow}}{\pi},$$

$$e_{z=z^*} = \frac{1-\sigma(x,y)}{1+\sigma(x,y)}\, h\beta_e, \quad f_{z=z^*} = 3q\beta_e\mu_0 e^{-\tau} + \frac{h\beta_e F_0^{\downarrow}(z=z^*)\sigma(x,y)}{\pi[1+\sigma(x,y)]},$$

where $F_0^{\downarrow}(z = z^*)$ is the direct solar irradiance at the surface.

For the lateral boundaries, we have the option of implementing open, isolated, or periodic boundary condition.

(1) *Open lateral boundary condition*. This condition imposes the radiation field on the boundary to be 2D, i.e., at lateral boundaries, the radiation field does not vary in the direction normal to the surface. Let x_a and x_b be the x-direction boundaries, and y_c and y_d be the y-direction boundaries, the radiation field is then homogeneous in the x- and y-directions such that

$$\left[\frac{\partial I_0^0}{\partial x_i}\right]_{x_i=\binom{x_{ia}}{x_{ib}}} = [3q\beta_e\Omega_{x_i 0}e^{-\tau_s}]_{x_i=\binom{x_{ia}}{x_{ib}}}, \tag{7}$$

where $i = 1, 2$, $x_1 = x$, $x_2 = y$, $\Omega_{x_1 0} = \Omega_{x0} = (1-\mu_0^2)^{1/2}\cos\phi_0$, $\Omega_{x_2 0} = \Omega_{y0} = (1-\mu_0^2)^{1/2}\sin\phi_0$, $x_{1a} = x_a$, $x_{1b} = x_b$, $x_{2a} = y_c$, $x_{2b} = y_d$, and μ_0, ϕ_0 are the cosine of the solar zenith and the solar azimuth angles, respectively.

(2) *Isolated lateral boundary condition*. Under this condition, there is no diffuse radiation propagating into the domain from outside. This can be achieved by setting the appropriate lateral fluxes to be 0 so that

$$\left[\frac{\partial I_0^0}{\partial x_i} \mp h\beta_e I_0^0\right]_{x_i=\binom{x_{ia}}{x_{ib}}} = [3q\beta_e\Omega_{x_i 0}e^{-\tau_s}]_{x_i=\binom{x_{ia}}{x_{ib}}}. \tag{8}$$

(3) *Periodic boundary condition*. In this case, the flux is assumed to be periodic on the lateral boundaries, where the diffuse radiation propagating outside the domain from x_b is equal to that propagating into the domain from x_a. Likewise, the same condition applies to the flux from x_a to outside, and from outside into x_b such that $F_{x=x_b}^{\rightarrow} = F_{x=x_a}^{\rightarrow}$ and $F_{x=x_a}^{\leftarrow} = F_{x=x_b}^{\leftarrow}$ (i.e., $I_0^0(x + x_b - x_a, y, z) = I_0^0(x, y, z)$ for all x, y, z). For the y-direction, we have $I_0^0(x, y + y_d - y_c, z) = I_0^0(x, y, z)$ for all x, y, z. Note that for different boundary conditions, a consistent approach must be used to calculate the optical depth along the solar direct beam.

2.2.2. Thermal infrared radiation boundary conditions

For thermal infrared radiation, the upward/downward fluxes are similar to Eq. (5) except that the last term vanishes. We can use the same vertical boundary conditions as in Eq. (6), except that the coefficients should be

$$e_{z=0} = -h\beta_e, \quad f_{z=0} = \frac{h\beta_e F^{\downarrow}_{top}}{\pi},$$

$$e_{z=z^*} = \frac{\varepsilon(x,y)}{2-\varepsilon(x,y)} h\beta_e, \quad f_{z=z^*} = \frac{\varepsilon(x,y) h\beta_e B[T_s(x,y)]}{2-\varepsilon(x,y)}.$$

Here $F^{\downarrow}_{top}$ is the incident downward diffuse infrared flux, and $\varepsilon(x,y)$ and $T_s(x,y)$ are the surface emissivity and surface temperature, respectively. As in the case of solar radiation, we may choose the following three different boundary conditions for lateral boundaries: (1) open lateral boundary condition in which the right-hand side (RHS) of Eq. (7) is 0; (2) isolated lateral boundary condition in which the RHS of Eq. (8) is 0; and (3) periodic boundary condition, which is the same as in the solar radiation case.

3. The full multigrid method

In Gu and Liou [5], the general second-order partial differential equation (PDE) shown in Eq. (2) was solved with the successive over-relaxation (SOR) method. Although SOR is straightforward for implementation, it has a problem of convergence when a sharp internal discontinuity occurs. For this reason, we have developed a new numerical approach based on the multigrid method [13–15]. This method can speed up the convergence by solving the PDE on a series of coarser grids first and then interpolating the coarse-grid corrections back to the pre-specified fine grids. Considerable computer time can be saved by carrying out major computational work on coarse grids. A signal having a low frequency on a fine grid $\tilde{u}_h$ will take substantial iterations for convergence by using the traditional relaxation methods (e.g., Jacobi, Gauss-Seidel). However, if we represent the same signal on a coarsened grid with a mesh size $H = 2h$ as $\tilde{u}_H$, this signal has a relatively higher frequency and converges more rapidly. Therefore, in the multigrid method, the high frequency errors are relaxed onto the fine grid and the low frequency errors are relaxed onto the coarse grid.

The PDE in Eq. (2) can be rewritten as follows:

$$\nabla^2 I_0^0 - \frac{1}{\beta_t}(\nabla\beta_t \cdot \nabla I_0^0) - 3\alpha_t\beta_t I_0^0 = \beta_t[-F_t + \mathbf{\Omega}_0 \cdot \nabla(F_t g/\beta_t)]. \tag{9}$$

With the appropriate boundary conditions on the domain, $[x_a, x_b]$, $[y_c, y_d]$, and $[z_e, z_f]$, we can define a linear second-order elliptic differential operator, $\mathbf{L}$, such that Eq. (9) can be expressed in the form

$$\mathbf{L} I_0^0 = f, \tag{10}$$

where f is the RHS of Eq. (9). Assuming that an equally spaced $n \times m \times l$ grid is superimposed on the domain and letting

$$\Delta x = \frac{x_b - x_a}{n-1}, \quad \Delta y = \frac{y_d - y_c}{m-1}, \quad \Delta z = \frac{z_f - z_e}{l-1}$$

be uniform grid increments in the x-, y-, and z-directions, respectively, we can implement the second-order central differencing scheme for all differentiation terms in the forms

$$\frac{\partial^2 I_0^0}{\partial x^2} = \frac{I_0^0(i+1,*) - 2I_0^0(i,*) + I_0^0(i-1,*)}{(\Delta x)^2}, \tag{11}$$

$$\frac{\partial I_0^0}{\partial x} = \frac{I_0^0(i+1,*) - I_0^0(i-1,*)}{2\Delta x}. \tag{12}$$

In Eqs. (11) and (12), the symbol "$*$" is used to represent the other two dimensions. At the boundary, we may add the "virtual" points to the center differencing formula by introducing a variable, $x(0) = x_a - \Delta x$. We then have

$$\left[\frac{\partial I_0^0}{\partial x}\right]_{x=x_a} = \frac{I_0^0(2,*) - I_0^0(0,*)}{2\Delta x} \tag{13}$$

in the x-direction boundary, $x = x_a$. In this manner, the unknown $I_0^0(0,*)$, which is determined from the discretization of the boundary condition equation, can be eliminated from the discretization of Eq. (9).

There are many elements in the multigrid method that can be employed for efficient solution involving the inhomogeneous partial differential equation. The first is associated with "discretization" and "finest grid" both of which strongly depend on the differential operators and the domain involved. In our problem, the unknowns I_0^0 are placed at the intersections of grid lines.

The second is related to the "smoothing operator $\mathbf{S}$" (the relaxation operator), which is the most important operator in the multigrid method. Its role is to damp the high frequency component of the errors on current grids, while remove the low frequency component of the errors on coarser grids. For the strongly anisotropic diffusion-absorption problem considered in this study, we use the block oriented scheme referred to as the alternating direction (AD) ZEBRA relaxation as the smoother. This scheme is highly recommended for solving anisotropic problems [15] to assure a sufficient smoothing effect. The ZEBRA relaxation scans the even-numbered blocks first and subsequently the odd-numbered blocks. It has been shown that block oriented schemes reduce the number of the required iteration for a fixed accuracy compared to the point relaxation method, which leads to a guaranteed convergence for the radiative transfer problem in multigrid iterations. The number $v = v_1 + v_2$ of relaxations representing the number of pre- and post-smoothing steps on the current level may be predefined.

The third is associated with "cycle". In the multigrid method, one iteration from the finest grid to the coarser grid, and back to the finest grid again, is called a cycle. The exact structure of a cycle depends on the recursion parameter γ, which is the number of two-grid iterations at each intermediate stage, greater or equal to one. With $\gamma = 1$, the so-called V-cycle is generated, while $\gamma = 2$ leads to the W-cycle. With the fixed values v_1 and v_2, the cycle is denoted as $\mathrm{V}(v_1, v_2)$ or $\mathrm{W}(v_1, v_2)$. The four level structure of the V- and W-cycles is illustrated in Fig. 1. In this study, we

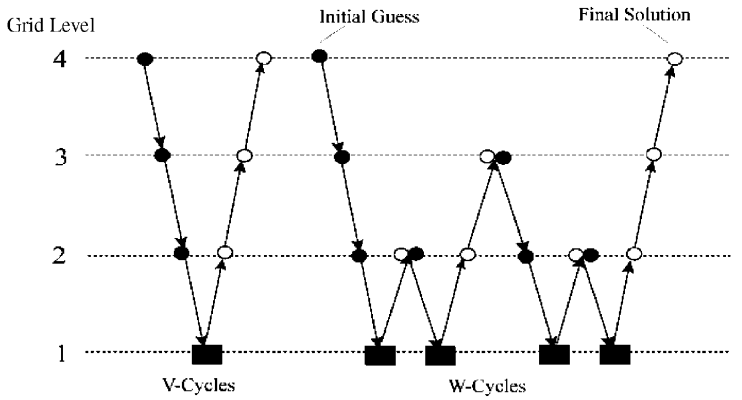

Fig. 1. The structure of V- and W-cycles in the full multigrid method. In the diagram, • denotes pre-smoothing steps, ○ denotes post-smoothing steps, ↑ denotes prolongation, ↓ denotes restriction, and ■ denotes direct solver.

used W (2,1) because it is more robust than the V-cycle in which γ determines in a certain sense the accuracy of the coarse grid correction.

The final one is related to the "restriction operator **R**" and "prolongation operator **P**". The proper choice of both the residual restriction and prolongation plays a key-role in the successful development of the multigrid method. The 27-point fully weighted residual restriction is used in this study, which is actually a natural extension from the 2D 9-point full weighting restriction to 3D space. The restriction **R** is defined by [16]

$$\mathbf{R}\, d_h(x,y,z) = \sum_{\alpha,\beta,\eta=-1}^{+1} \sigma_{\alpha\beta\eta} d_h(x+\alpha\Delta x, y+\beta\Delta y, z+\eta\Delta z), \tag{14}$$

where

$$\sigma_{\alpha\beta\eta} = \begin{cases} 1/8 & \text{if } \alpha=\beta=\eta=0, \\ 1/16 & \text{if } |\alpha|+|\beta|+|\eta|=1, \\ 1/32 & \text{if } |\alpha|+|\beta|+|\eta|=2, \\ 1/64 & \text{if } |\alpha|+|\beta|+|\eta|=3. \end{cases} \tag{15}$$

In this manner, the weighting satisfies the conservation property of the integrals. The transformation from a coarse grid to the next finer one, i.e., prolongating the correction, is usually done by interpolation. The multicubic interpolation in 3D space is sufficient for our problem, which is a 4th order problem and is greater than the order of the differential operator (2nd order).

4. Computational results and discussions

We first compare the results computed from the multigrid method with those from the SOR method presented in Gu and Liou [5] to ensure the results are the same for the cases presented in that paper. In that paper, validation of the 3D delta-diffusion radiative transfer model employing

the SOR approach has been performed extensively, including comparisons of the model results to those from the plane-parallel (PP) method, the successive-orders-of-scattering method [10], and the spherical harmonics discrete-ordinates method [11]. Excellent agreements for both the broadband and monochromatic results have been demonstrated. In these comparisons, the broadband radiative transfer calculation is performed by using six solar bands with 54 correlated k-distribution and 12 thermal infrared bands with 67 correlated k-distribution [17,18], the same spectral divisions as in Gu and Liou [5]. A 3D homogeneous cirrus cloud field was constructed with a uniform ice water content value of $0.015\,g/m^3$ and a mean effective ice crystal size of 25 μm. The cloud was located between 7 and 11 km in a standard midlatitude winter atmosphere and had a dimension of 4 km in the x, y, and z directions. A uniform grid with 33 points was used in the cloud for each of the three directions resulting in a 0.125 km resolution. The cloud-top and base temperatures were fixed at 219.2, and 238.5 K, respectively, while a surface temperature of 272.2 K was used. The solar zenith angle used was set at 60° and the solar beam propagation was directly toward the positive x direction. The cloud optical properties, including the extinction coefficient, the single-scattering albedo, and the asymmetry factor, were parameterized in terms of the ice water content and mean effective ice crystal size [19]. The delta-function adjustment was also used to account for the strong forward-diffraction nature in the phase function of cloud particles to enhance computational accuracy.

We subsequently carry out comparison of the heating fields produced by different boundary conditions, which have not been considered in Gu and Liou [5]. The domain-average (i.e., averaged over the x, y, and z directions) broadband radiative heating rates for a cloud with a relative dimension of 1/1/1 computed from the present 3D model and a PP program are presented in Fig. 2. A strong solar heating in the cloud, which increases with the cloud height, is shown. On the other hand, there is a strong IR cooling at the cloud top with a substantial warming at the cloud bottom. For the horizontal open boundary condition (dash line), the heating rates computed from the 3D model are very close to those computed from the PP program for both

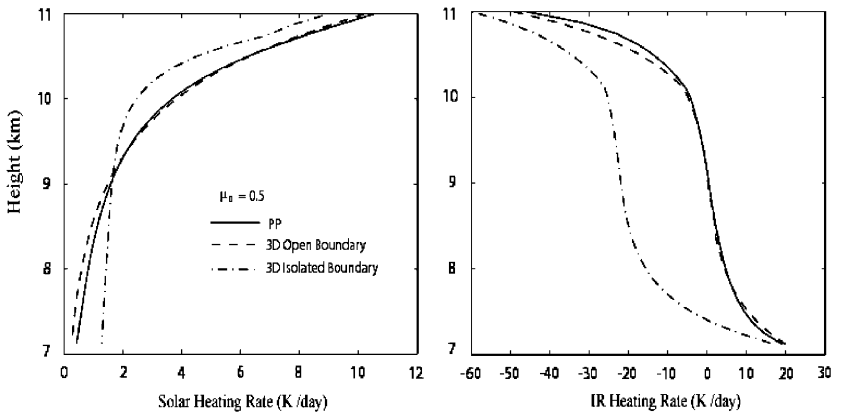

Fig. 2. Comparison of the broadband solar and thermal infrared heating rates computed from the present 3D delta-diffusion model with open and isolated boundary conditions (see text for definitions) and the plane-parallel method for a homogeneous cirrus cloud layer.

solar and infrared radiation, which is not surprising since the cloud extends to infinity in the horizontal direction under the open boundary condition. In this case, the 3D homogeneous cloud field can be treated as the PP cloud. For the isolated boundary condition, leaking of photons from the side surfaces results in a smaller solar heating rate in the upper portion of the cloud (above 9 km) for the 3D model as compared to the PP results. The 3D heating rate is greater than the PP counterpart at the lower portion of cloud (below 9 km). This is because the attenuation of the direct solar beam does not occur for the facing boundaries (*yz* plane) so that the input photons at these boundaries are stronger than those of other boundaries. For thermal infrared radiation, the cooling rate from the present 3D model is much greater than the PP results for the isolated boundary condition (dash–dot line) due to the following reasons: (1) there are no diffuse fluxes input from the outside to the domain; (2) there are no thermal infrared emission from the outside to the domain; and (3) the photons (scattering and direct emission) leaving the domain do not return. For these reasons, large cooling rates at the boundary are present, which have a great impact on the domain-average value.

Finally, we compare the solar heating rate results computed from the present delta-diffusion model to those computed from the broadband solar Monte Carlo method [20]. For this comparison, we use the optical depth and mean effective ice crystal size over an area of 30 km by 20 km near Coffeyville, Kansas, on 5 December 1991, retrieved from the advanced very high resolution radiometer (AVHRR) presented in Gu and Liou [5]. The cloud thickness used is 2 km. The 3D extinction coefficient field can then be constructed from the optical depth and mean effective ice crystal size for input to radiative transfer models. Base on the multigrid method, the 3D cirrus field is divided to produce a pattern consisting of $29 \times 17 \times 9$ grid points. With the domain defined in Fig. 3(a), the resolution for each point is 1 km × 1 km × 0.25 km. Because of the difficulty in visualizing the 3D results, we have presented them in the *xy, xz,* and *yz* planes. Value of the IWC varies from about 1–7 mg/m^3, revealing that this cloud is highly inhomogeneous in both the vertical and horizontal directions. Fig. 3(b) displayed the solar heating rates in the *xy, yz* and *xz* planes computed from the present 3D model. The heating rates range from about 1 to 2.2 K/day and its pattern is correlated with the extinction coefficient or IWC: stronger (weaker) heating rates correspond to larger (smaller) extinction coefficients. For comparison, Fig. 3(c) shows the "exact" results computed from the Monte Carlo method. The solar heating rate patterns computed from these two methods are strikingly similar. Absolute differences between the two range from −0.08 to 0.08 K/day with a percentage difference less than about 5%. In the *xy* plane, we find the delta-diffusion model produces less heating compared to that from the Monte Carlo method in the area where IWC is large. On the other hand, the reverse is true for the heating rate near the cloud bottom. This comparison and those not presented in this paper demonstrate that the delta-diffusion model is indeed an excellent approximation for the calculation of 3D radiative transfer in inhomogeneous medium. A final note regarding the compute time is in order. For the preceding calculations, the present delta-diffusion model with the $29 \times 17 \times 9$ grid point domain took only 3 min to complete on a SUN workstation, whereas with the same grid point configuration, the Monte Carlo method requires about 7 h to achieve the converged result (using 500 000 K photons) on the same computer.

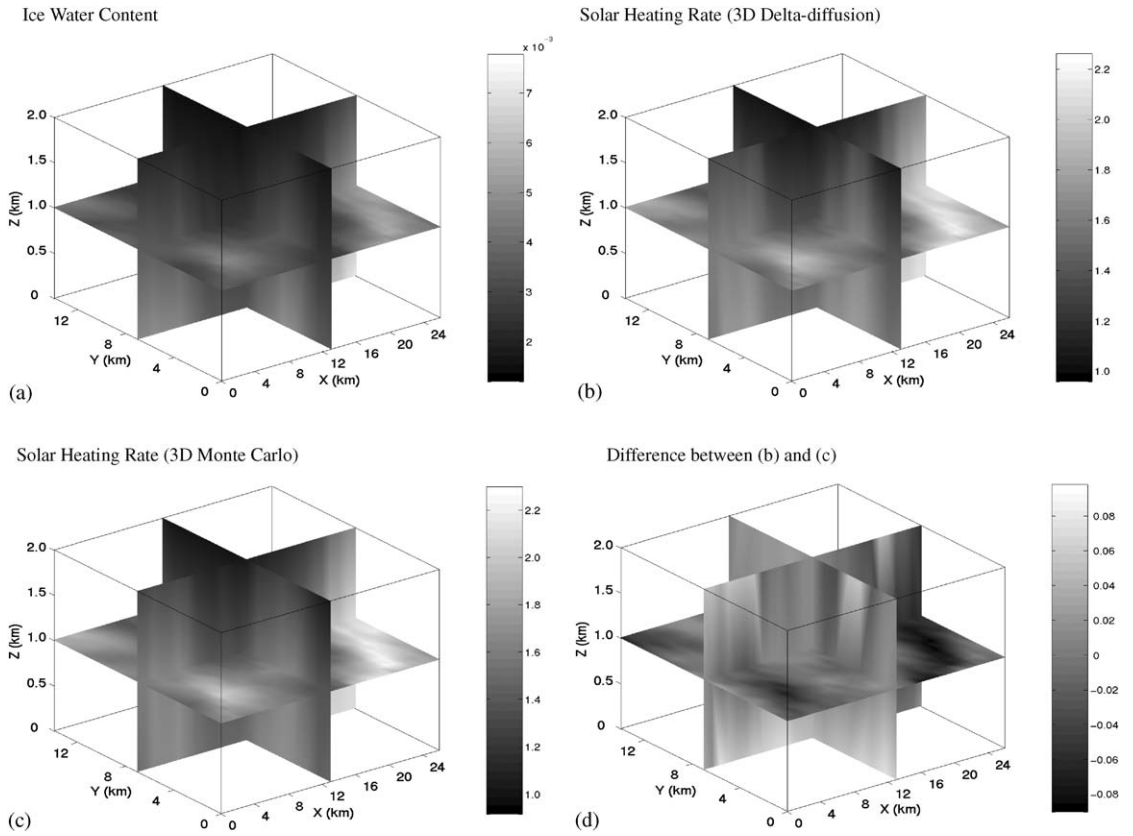

Fig. 3. 3D images for (a) ice water content (g/m^3) (after Gu and Liou [5]), (b) solar heating rates in K/day computed from the 3D delta-diffusion model, (c) solar heating rates computed from the 3D Monte Carlo method, and (d) solar heating rate differences between (b) and (c). The 3D results are presented in the *xy*, *yz*, and *xz* planes over a 27 km × 15 km × 2 km domain.

5. Conclusions

In this paper, we have solved the 3D inhomogeneous diffuse radiative transfer equation based on the full multigrid method. It is a differential method that can be applied to specific geometry with different boundary conditions imposed and can adequately account for sharp boundary discontinuity. We have used the Cartesian coordinate systems in solving the transfer of both solar and thermal infrared radiation employing discretized spatial grids. The accuracies of the 3D delta-diffusion model are first checked with the results presented in Gu and Liou [5] who used the over-relaxation method for the solution. Subsequently, we compared the present model results using different boundary conditions with those computed from the 1D plane-parallel method in terms of solar and infrared heating rates in a homogeneous cloud layer. We showed that the present 3D model with the open boundary condition gives similar results to those calculated from the plane-parallel method.

We then compare the solar heating rates for a 3D inhomogeneous cirrus cloud layer constructed from remote sensing based on the 3D delta-diffusion model and the "exact" Monte Carlo method with the same input parameters. We found that the results computed from the former are within about 5% of those computed from the latter, which requires a much large computational effort to achieve the convergence. The present 3D delta-diffusion model for radiative transfer in 3D inhomogeneous clouds based on the full multigrid numerical method is computational efficient and is ideal for use in radiative transfer parameterization involving finite and inhomogeneous clouds and aerosols in climate models.

Acknowledgements

This work has been supported by DOE Grant DE-FG02-04ER6333724 and NSF Grants ATM-9907924 and ATM-0331550. We thank Professor Q. Fu from the University of Washington for providing us the Monte Carlo code in conjunction with this study.

References

[1] Cahalan R, Ridgway W, Wiscombe WJ, Gollmer S, Harshvardhan. Independent pixel and Monte Carlo estimates of stratocumulus albedo. J Atmos Sci 1994;51:3776–90.
[2] Welch RM, Wielicki BA. Stratocumulus cloud field reflected fluxes: the effect of cloud shape. J Atmos Sci 1984;41:3085–103.
[3] Barker HW. Solar radiative transfer for clouds possessing isotropic variable extinction coefficient. Q J R Meteorol Soc 1992;118:1145–62.
[4] Barker HW, Morcrette JJ, Alexander GD. Broadband solar fluxes and heating rates for atmospheres with 3D broken clouds. Q J R Meteorol Soc 1998;124:1245–71.
[5] Gu Y, Liou KN. Radiation parameterization for three-dimensional inhomogeneous cirrus clouds: application to climate models. J Clim 2001;14:2443–57.
[6] Liou KN, Ou SC. Infrared radiative transfer in finite cloud layers. J Atmos Sci 1979;36:1985–96.
[7] Ou SC, Liou KN. Generalization of the spherical harmonic method to radiative transfer in multi-dimensional space. JQSRT 1982;28:271–88.
[8] Evans KF. Two-dimensional radiative transfer in cloudy atmospheres: the spherical harmonic spatial grid method. J Atmos Sci 1993;50:3111–24.
[9] Gabriel PM, Tsay SC, Stephens GL. A fourier-riccati approach to radiative transfer. Part I: Foundations. J Atmos Sci 1993;50:3125–47.
[10] Liou KN, Rao N. Radiative transfer in cirrus clouds. Part IV: On cloud geometry, inhomogeneity and absorption. J Atmos Sci 1996;53:3046–65.
[11] Evans KF. The spherical harmonics discrete ordinate method for three-dimensional atmospheric radiative transfer. J Atmos Sci 1998;55:429–46.
[12] Liou KN. An introduction to atmospheric radiation, 2nd ed. New York: Academic Press; 2002.
[13] Brandt A. Multi-level adaptive solutions to boundary value problems. Math Comp 1977;31:333–90.
[14] Hackbusch W. Multi-grid methods and applications. Berlin: Springer; 1985.
[15] Joppich W, Mijalkovic S. Multigrid methods for process simulation. Berlin: Springer; 1993.
[16] Z. Qu. On the transfer of ultraviolet radiation in horizontally inhomogeneous atmospheres: a three dimensional approach based on the delta-Eddington's approximation. Ph.D. thesis. University of Chicago, 1999.
[17] Fu Q, Liou KN. On the correlated k-distribution method for radiative transfer in nonhomogeneous atmospheres. J Atmos Sci 1992;49:2139–56.

[18] Fu Q, Liou KN. Parameterization of the radiative properties of cirrus clouds. J Atmos Sci 1993;50:2008–25.
[19] Fu Q. An accurate parameterization of the solar radiative properties of cirrus clouds for climate models. J Clim 1996;9:2058–82.
[20] Fu Q, Cribb MC, Barker HW, Krueger SK, Grossman A. Cloud geometry effects on atmospheric solar absorption. J Atmos Sci 2000;57:1156–68.